Analytical description of free-electron-laser oscillations in a perfectly synchronized optical cavity

Nobuyuki Nishimori*

Advanced Photon Source Center, Japan Atomic Energy Agency (JAEA), Tokai, Naka, Ibaraki 319-1195, Japan

(Received 23 April 2003; revised manuscript received 10 April 2006; published 13 September 2006)

We present an analytical description of free-electron-laser (FEL) oscillations in a perfectly synchronized optical cavity by solving the one-dimensional FEL equations. It is shown that the radiation stored in the cavity eventually evolves into an intense few-cycle optical pulse in the high-gain and low-loss regime despite the lethargy effect. The evolution of the leading slope of the optical pulse, which is defined from the front edge toward the primary peak, is found to play an important role in generating the intense few-cycle optical pulse. The phase space evolution of electrons which interact with the leading slope is solved analytically in a perturbation method, leading to an analytical solution for the optical pulse evolution. The peak amplitude and the pulse length at saturation are found to scale with the electron beam density and optical cavity loss. Those scalings agree well with the intense few-cycle pulses recently observed in a high-power FEL.

DOI: 10.1103/PhysRevE.74.036502 PACS number(s): 41.60.Cr

I. INTRODUCTION

A free-electron laser (FEL) is one of the most important coherent sources of radiation. It can produce intense, ultrashort laser pulses at any wavelength. These unique capabilities will open up new research fields in chemical, biological, and material science [1], e.g., quantum control of atomic and molecular states [2].

The FEL dynamics is affected by the slippage that is caused by the velocity difference between the electron bunch and the optical pulse inside an undulator. The group velocity of the optical pulse becomes slightly slower than the vacuum speed of light, since the trailing slope of the optical pulse is mainly amplified due to the slippage. This phenomenon, called the laser lethargy (see Ref. [3] and references therein), can be compensated in oscillators by slightly shortening the optical cavity length from the perfect synchronism ($\delta L=0$), where the cavity length exactly matches with the injection period of the electron bunches. The FEL dynamics of the oscillators with shorter cavity length ($\delta L<0$) has been studied extensively [4,5]. At $\delta L=0$, the optical pulse centroid continues to be retarded on successive passes through the undulator, and the optical pulse finally dissipates, as shown in theoretical studies [6–8].

The parameters used in the above theoretical studies for FELs at $\delta L=0$ are similar to those of the first FEL oscillation at Stanford University [9], where Colson's dimensionless current $j_0=2(4\pi\rho N_w)^3$ was a small value, $j_0=5$ [6]. Here ρ is the fundamental FEL parameter proportional to the cubic root of the electron beam density n_e [10], and N_w is the number of undulator periods. After the first FEL oscillation, high-gain FEL oscillators with $j_0 \gg 5$ such as FELIX [11] have been developed worldwide, but no experimental observation of lasing at $\delta L=0$ was reported until recently. A possible reason is that the number of interactions between the round-trip optical pulse and incident electron bunches was restricted to a few hundreds, since normal conducting linacs operating in the *L* or *S* band were used as driver accelerators for the high-gain oscillators.

The development of a high-power FEL driven by a superconducting linac has resulted in a FEL operating in the high-gain regime such as $j_0=50$ with pass number greater than 1000, at the Japan Atomic Energy Research Institute (JAERI) FEL facility [12]. An experiment at the JAERI FEL showed that an intense, ultrashort optical pulse was generated at $\delta L=0.0\pm0.1$ μm despite the lethargy [12,13]. The optical power curve measured with respect to δL is well reproduced by the time-dependent simulation code based on one-dimensional (1D) FEL equations [14], if shot-noise effect is included in every fresh electron bunch as suggested by Brau [15]. A few theoretical studies have attempted to explain the FEL oscillation at $\delta L=0$, proposing that sideband instability [16] or superradiance in short-pulse FELs [17] is the fundamental physics responsible for the lasing at $\delta L=0$. Nevertheless, the underlying physics responsible for the FEL oscillation at $\delta L=0$ has not been clearly explained yet.

A distinguishing feature of the oscillation at $\delta L=0$ from those where $\delta L<0$ is that the amplitude of the optical pulse increases exponentially along the leading slope, which is defined from the front edge toward the primary peak amplitude in the present paper. The amplitude at the front edge remains at the spontaneous emission level, since the position of the front edge is the same as that of every incident electron bunch at the entrance to the undulator [18]. The optical pulse energy is mainly carried by the primary peak area at saturation [14] and the leading slope of the FEL pulse plays an important role in the FEL oscillation at $\delta L=0$. The intensity gradient of the leading slope with respect to the longitudinal position increases with the pass number *n* and the optical field is sustained in saturation, as shown in a numerical simulation (see Sec. III). These features of the oscillation at $\delta L=0$ observed in the simulation cannot be explained by the shot-noise effect only.

In this paper, we investigate the FEL evolution and saturation at $\delta L=0$ by analytically solving the 1D FEL equations. A set of nondimensional parameters and the 1D FEL equations described in Sec. II are employed for the present study. The optical pulse on the first pass, which is equivalent to the output of a self-amplified spontaneous-emission (SASE) FEL and represented by the solution of the cubic equation [10,19,20], is reflected back into the undulator for subse-

*Electronic address: nishimori.nobuyuki@jaea.go.jp

quent amplifications in FEL oscillators. The phase space evolution of electrons on the second pass that interact with the leading slope of the FEL pulse is obtained in a perturbation method similar to that used in our previous work for the phase space evolution of electrons in a SASE FEL [21], which is briefly described in Sec. IV. Consequently, an analytical solution for the optical growth of the leading slope during the second pass is derived. The leading slope of the output pulse is shown to be approximated by that of a SASE FEL with FEL parameter greater than ρ in Sec. V. The same process can thus be applied to pass numbers greater than $n=2$ and the evolution of the leading slope with respect to n is obtained analytically. The output field similar to that of a SASE FEL accounts for the exponential increase of the field amplitude in the leading slope from the front edge toward the primary peak, and the amplitude gradient with respect to the longitudinal position is shown to increase with n. With the increasing gradient, the field gain per pass decreases down to the level of optical cavity loss α, and a self-similar radiation pulse is generated at saturation (see Sec. VI), as already seen in our previous numerical simulation [14]. The evolution of the leading slope leads to sustained FEL oscillations at $\delta L=0$ and thus disappearance of the lethargy effect. The peak intensity of the intracavity radiation field in saturation is found to reach approximately $37\alpha^{-4/3}$ times higher than that of a long-pulse SASE FEL with the same ρ. The pulse length is shown to be given by $0.036\alpha^{1/3}/\rho$ in units of FEL wavelength, which can go down to a few wavelength cycles in the regime of high-electron-beam density ρ and low loss α. The peak intensity and pulse length obtained in the present study agree well with experiments performed at the JAERI FEL (see Sec. VII). Finally, our conclusions are given in Sec. VIII.

II. 1D FEL EQUATIONS

A relativistic electron beam traveling through an undulator emits spontaneous radiation along the undulator axis. The bandwidth of the radiation field decreases due to the spectrum narrowing as the beam passes through the undulator [6]. The field within the bandwidth is then amplified by interacting with the undulating electrons. The electron dynamics in the radiation field and evolution of the laser field are represented by 1D FEL equations [6,15].

The dimensionless 1D FEL equations of Colson are used in the present study under the slowly varying envelope approximation [22], while the variables used here are similar to Bonifacio's variables [10]. The simplest situation is considered in the present study. The electron beam energy is given by $\gamma_0 mc^2$ with small energy spread. The initial electron bunch has a rectangular shape with density of n_e and a uniform distribution in phase. The fundamental FEL parameter in MKSA units is given by

$$\rho = \frac{1}{\gamma_0}[ea_w F\sqrt{n_e/(\varepsilon_0 m)}/(4ck_w)]^{2/3}. \tag{1}$$

Here $\lambda_w=2\pi/k_w$ is the period of the undulator, a_w is the undulator parameter, and F is unity for a helical undulator or a Bessel function $[JJ]$ for a planar undulator [10]. The dimensionless time is defined by $\tau=4\pi\rho ct/\lambda_w$, so that $\delta\tau=1$ corresponds to the transit time of light through one gain length of $\lambda_w/(4\pi\rho)$. The longitudinal position of the ith electron is defined by $\zeta_i(\tau)=4\pi\rho[z_i(t)-ct]/\lambda_r$, so that $\delta\zeta=1$ corresponds to the cooperation length defined by $L_c=\lambda_r/(4\pi\rho)$. Here $\lambda_r=\lambda_w(1+a_w^2)/(2\gamma_0^2)$ is the resonant wavelength. The dimensionless field envelope is defined by

$$a(\zeta,\tau) = \frac{2\pi e a_w \lambda_w F}{(4\pi\rho)^2\gamma_0^2 mc^2}E(\zeta,\tau)\exp[i\phi(\zeta,\tau)], \tag{2}$$

with phase $\phi(\zeta,\tau)$, which is equivalent to Bonifacio's envelope [10]. Here $E(\zeta,\tau)$ is the rms optical field strength. The dimensionless energy and phase of the ith electron are respectively defined by $\mu_i(\tau)=[\gamma_i(t)-\gamma_0]/(\rho\gamma_0)$ and $\psi_i(\tau)=(k_w+k_r)z_i(t)-\omega_r t$, where $k_r=2\pi/\lambda_r$ is the wave number of the resonant wavelength λ_r. The dimensionless energy $\mu_i(\tau)$ also means the dimensionless energy change at τ from $\tau=0$, since the energy spread of the initial electron beam is assumed to be small, i.e., $\mu_i(0)=0$.

In the present definition, the evolutions of the field envelope $a(\zeta,\tau)$, the energy $\mu_i(\tau)$, and the phase $\psi_i(\tau)$ of the ith electron during FEL interaction are respectively given by [6]

$$\frac{d\mu_i(\tau)}{d\tau} = a[\zeta_i(\tau),\tau]\exp[i\psi_i(\tau)] + \text{c.c.}, \tag{3}$$

$$\frac{d\psi_i(\tau)}{d\tau} = \mu_i(\tau), \tag{4}$$

$$\frac{\partial a(\zeta,\tau)}{\partial\tau} = -\langle\exp[-i\psi_i(\tau)]\rangle_{\zeta_i(\tau)=\zeta}. \tag{5}$$

The angular brackets indicate the average of all the electrons in the volume V around ζ.

III. NUMERICAL SIMULATIONS

Our numerical simulations, which solve the time-dependent 1D FEL equations with the macroparticle model [15,14], have already reproduced the FEL efficiency curve measured at the JAERI FEL as a function of δL [12]. The macroparticle model allows us to easily deal with the shot noise of an electron bunch. A method developed by Penman and McNeil has been employed in the simulations to give an appropriate shot-noise effect by compensating for the limited number of macroparticles [23]. The number of macroparticles used is 100 for every resonant wavelength λ_r and the typical electron bunch length is $100\lambda_r$, which corresponds to $400\pi\rho$ in units of L_c. The optical field is described at points separated by λ_r. The time evolutions of the optical field and the phase space of electrons are calculated every $\delta\tau=4\pi\rho$ from Eqs. (3)–(5) and are integrated over the whole undulator length in a similar way as described in Refs. [14,15].

One of the most important conclusions of our previous numerical simulations is that the small shot noise needs to be included in every fresh electron bunch to reproduce the high extraction efficiency at zero detuning length of an optical cavity observed at the JAERI FEL [14]. On the other hand,

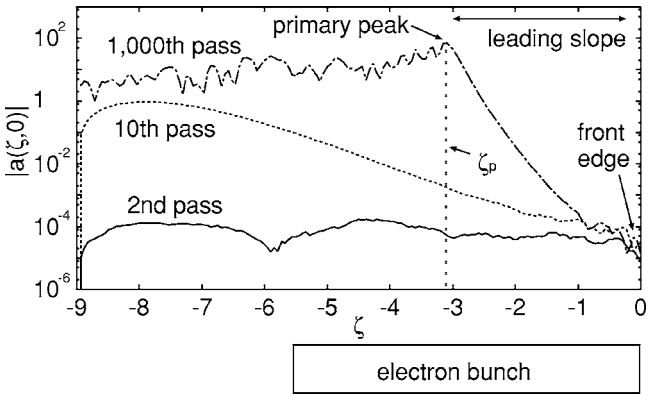

FIG. 1. Temporal profiles of optical amplitudes $|a(\zeta,0)|$ at $\delta L=0$ on the second (solid line), tenth (dotted line), and 1000th passes (dash-dotted line) plotted on a semilogarithmic scale. The position of the incident electron bunch at the entrance to an undulator is schematically shown as well. The parameters in the simulation are $\rho=0.0045$, $L_b=5.6$, $L_s=3.4$, and the optical cavity loss $\alpha=0.05$.

the simulations also show that a distinguishing feature of the oscillation at $\delta L=0$ from those where $\delta L<0$ is that the amplitude of the optical pulse increases exponentially along the leading slope from the front edge toward the primary peak amplitude, while the amplitude at the front edge remains at the spontaneous emission level [18]. The intensity gradient of the leading slope with respect to the longitudinal position increases with pass number n and the optical field is sustained in saturation, as shown in Fig. 1, which depicts the temporal profiles of optical amplitudes with respect to ζ on a semilogarithmic scale obtained in the simulation at the entrance to the undulator on the second, tenth, and 1000th passes. These features of the oscillation at $\delta L=0$ cannot be explained by the shot-noise effect only. The incident electron bunch used in the simulations has a length of L_b and a constant FEL parameter ρ independent of ζ. Both L_b and the slippage distance $L_s=4\pi\rho N_w$ in units of L_c are longer than the distance from $\zeta=0$ to the peak position at saturation, ζ_p. Here $\zeta=0$ stands for the front edge of the optical pulse and agrees with that of the incident electron bunch at the entrance to the undulator, and ζ_p represents the position of the primary peak amplitude of the optical pulse. The region from $\zeta=0$ to ζ_p is defined as the leading slope in the present paper.

The leading slope is similar to that in a high-gain SASE FEL [10]. In both cases, the amplitude at $\zeta=0$ is at the spontaneous emission level, while the subsequent portions of the amplitude increase exponentially with the distance from the front edge [18]. The gradient of the amplitude increases along with the pass number n and is kept almost constant in saturation. This evolution of the leading slope as well as the phase space evolution of electrons are analyzed in Secs. IV and V.

IV. OPTICAL FIELD AND ELECTRON PHASE SPACE EVOLUTIONS ON THE FIRST PASS

The optical field and electron phase space evolutions on the first pass, which are equivalent to those in a SASE FEL, are presented in our previous work [21] and summarized briefly in this section. The startup process known as spectrum narrowing in the frequency domain [24] or longitudinal phase mixing in the time domain [25] leads to a uniform field in time and space. The phase of the field $\phi(0)$ is almost uniform over the length $N\lambda_r$ along the propagation direction when the incident electron beam passes through N undulator periods [6,25]. In the present study, the initial uniform field is assumed to be given by $|a(0)|e^{i\phi(0)}$ for simplicity. The initial field evolves through electric interaction with undulating electrons as it passes through the undulator. The incident electron beam is assumed to be uniformly distributed in phase $\psi_i(0)$ with resonant energy $\mu_i(0)=0$ and interacts with the SASE FEL field in the steady-state region due to the slippage [10]. The evolution of the uniform field as a function of time is derived from Eqs. (3)–(5), as described by Colson *et al.* in Ref. [20].

The electron phase can be expressed as $\psi_i(\tau)=\psi_i(0)+\Delta\psi_i(\tau)$ where $\Delta\psi_i(\tau)$ is the first-order perturbation in $a(\tau)$. The field at time τ for the steady-state region where $\zeta<-\tau$ is given by

$$a(\tau)=a(0)+i\int_0^\tau \langle \exp[-i\psi_i(0)]\Delta\psi_i(\tau')\rangle_{\zeta_i(\tau)=\zeta} d\tau'. \quad (6)$$

The ith electron interacts with the field in the steady-state region due to the slippage, and the energy modulation at τ' during $\delta\tau'$ is given from Eq. (3) by $\delta\mu_i(\tau')=[a(\tau')e^{i\psi_i(0)}+\text{c.c.}]\delta\tau'$. The energy change of the ith electron at time τ, $\mu_i(\tau)$, is given by the sum of those modulations during τ:

$$\mu_i(\tau)=\int_0^\tau \{a(\tau')\exp[i\psi_i(0)]+\text{c.c.}\}d\tau'. \quad (7)$$

The electron phase perturbation is given from Eq. (4) by

$$\Delta\psi_i(\tau)=\int_0^\tau \mu_i(\tau')d\tau' \quad (8)$$

$$=\int_0^\tau d\tau' \int_0^{\tau'} \{a(\tau'')\exp[i\psi_i(0)]+\text{c.c.}\}d\tau''. \quad (9)$$

Substitution of Eq. (9) into Eq. (6) leads to

$$a(\tau)=a(0)+i\int_0^\tau d\tau' \int_0^{\tau'} d\tau'' \int_0^{\tau''} a(\tau''')d\tau'''. \quad (10)$$

The integral equation (10) can be written in a differential form by taking successive derivatives, $\dddot{a}(\tau)=ia(\tau)$. The solution is expressed in the form $a(\tau)=\Sigma_{n=1}^3 a_n \exp(\alpha_n\tau)$ where the α_n are three complex roots of the cubic equation $\alpha^3=i$ [10,19,20]. When the initial conditions $\dot{a}(0)=\ddot{a}(0)=0$, the field at time τ for the steady-state region where $\zeta<-\tau$ is given by

$$a(\tau) = \frac{|a(0)|e^{i\phi(0)}}{3}[\exp(\tau e^{i\pi/6}) + \exp(-\tau e^{-i\pi/6}) + \exp(\tau e^{-i\pi/2})], \quad (11)$$

where the first term is an exponentially growing term, the second term is an exponentially decaying term, and the third is an oscillating term. Equation (11) is valid in the linear regime before saturation when the incident electron beam is resonant.

The integration of Eq. (7) after substitution of Eq. (11) yields

$$\mu_i(\tau) = \frac{2|a(0)|}{3}\{e^{\sqrt{3}\tau/2}\cos[\psi_i(0) + \phi(0) + \tau/2 - \pi/6] - e^{-\sqrt{3}\tau/2}\cos[\psi_i(0) + \phi(0) + \tau/2 + \pi/6] + \cos[\psi_i(0) + \phi(0) - \tau + \pi/2]. \quad (12)$$

The integration of Eq. (8) after substitution of Eq. (12) yields

$$\Delta\psi_i(\tau) = \frac{2|a(0)|}{3}\{e^{\sqrt{3}\tau/2}\cos[\psi_i(0) + \phi(0) + \tau/2 - \pi/3] + e^{-\sqrt{3}\tau/2}\cos[\psi_i(0) + \phi(0) + \tau/2 + \pi/3] + \cos[\psi_i(0) + \phi(0) - \tau + \pi]. \quad (13)$$

Equations (12) and (13) are the analytical expressions for the phase space evolution of electrons in a SASE FEL operating in the linear regime [21]. The gain of the steady-state field at time τ is obtained by substitution of Eq. (13) into Eq. (5) as follows:

$$\frac{da(\tau)}{d\tau} = \frac{|a(0)|e^{i\phi(0)}}{3}[\exp(\tau e^{i\pi/6})e^{i\pi/6} - \exp(-\tau e^{-i\pi/6})e^{-i\pi/6} + \exp(\tau e^{-i\pi/2})e^{-i\pi/2}], \quad (14)$$

when $|\Delta\psi_i(\tau)| \ll 1$. Equation (14) is the same as differentiation of Eq. (11) with respect to τ.

V. OPTICAL FIELD AND ELECTRON PHASE SPACE EVOLUTIONS ON THE nTH PASS

In this section, we first study the optical field and electron phase space evolutions on the second pass ($n=2$) in an analytical way and then show that the analytical method can be applied to the nth pass with reasonable approximations. At first the notation n is thus used for $n=2$.

A. Optical field and electron phase space evolutions on the second pass

The input field for the second pass, $a_n(\zeta)=a_n(\zeta,0)$, is the same as the output of a SASE FEL with FEL parameter ρ except for a decrease of the amplitude due to the cavity loss α. The leading slope of the input field for the second pass is therefore given as a function of ζ by

$$a_n(\zeta) = \frac{|a_n(0)|e^{i\phi_n(0)}}{3}[\exp(-\rho_n\zeta e^{i\pi/6}) + \exp(\rho_n\zeta e^{-i\pi/6}) + \exp(-\rho_n\zeta e^{-i\pi/2})], \quad (15)$$

where $\rho_2=1$ and $|a_2(0)| \approx (1-\alpha/2)|a(0)|$. Equation (15) can be used where $|\zeta| < L_s$ and $|\zeta| < L_b$ before the field reaches saturation. The phase space evolution of electrons during interaction with the leading slope given by Eq. (15) is quite similar to that of a SASE FEL described in the preceding section, since the electrons with initial position ζ interact at time τ with a field represented by

$$\frac{|a_n(0)|e^{i\phi_n(0)}}{3}\{\exp[\rho_n(\tau-\zeta)e^{i\pi/6}] + \exp[-\rho_n(\tau-\zeta)e^{-i\pi/6}] + \exp[\rho_n(\tau-\zeta)e^{-i\pi/2}]\},$$

which is similar to Eq. (11). The perturbation method used in Sec. IV can be applied to a study of the optical growth during the second pass, as long as the growth is small and the field $a_n(\zeta)$ remains almost unchanged during the FEL interaction. The electron phase can be expressed as $\psi_i(\tau)=\psi_i(0) + \Delta\psi_i(\tau)$ where $\Delta\psi_i(\tau)$ is the first-order perturbation in $a_n[\zeta_i(\tau)]/\rho_n^2$, since the field in the leading slope divided by ρ_n^2 is weak even after saturation except for a narrow range near ζ_p (see Fig. 1). When the ith electron is modulated in energy by interacting with the leading slope, the energy modulation at τ' during $\delta\tau'$ is expressed from Eq. (3) by $\delta\mu_i(\tau') = \{a_n[\zeta_i(\tau')]e^{i\psi_i(0)} + \text{c.c.}\}\delta\tau'$. The energy change of the ith electron at time τ, $\mu_i(\tau)$, is given by the sum of those modulations during τ:

$$\mu_i(\tau) = \int_0^\tau \{a_n[\zeta_i(\tau')]\exp[i\psi_i(0)] + \text{c.c.}\}d\tau'. \quad (16)$$

The integration of Eq. (16) after substitution of Eq. (15) yields

$$\mu_i(\tau) = \frac{2|a_n(0)|}{3\rho_n}\{e^{-\sqrt{3}\rho_n\zeta_i(\tau)/2}\cos[\psi_i(0) + \phi_n(0) - \rho_n\zeta_i(\tau)/2 - \pi/6] - e^{-\sqrt{3}\rho_n\zeta_i(0)/2}\cos[\psi_i(0) + \phi_n(0) - \rho_n\zeta_i(0)/2 - \pi/6] - e^{\sqrt{3}\rho_n\zeta_i(\tau)/2}\cos[\psi_i(0) + \phi_n(0) - \rho_n\zeta_i(\tau)/2 + \pi/6] + e^{\sqrt{3}\rho_n\zeta_i(0)/2}\cos[\psi_i(0) + \phi_n(0) - \rho_n\zeta_i(0)/2 + \pi/6] + \cos[\psi_i(0) + \phi_n(0) + \rho_n\zeta_i(\tau) + \pi/2] - \cos[\psi_i(0) + \phi_n(0) + \rho_n\zeta_i(0) + \pi/2]\}. \quad (17)$$

The integration of Eq. (8) after substitution of Eq. (17) yields

$$\Delta\psi_i(\tau) = \frac{2|a_n(0)|}{3\rho_n^2}\{e^{-\sqrt{3}\rho_n\zeta_i(\tau)/2}\cos[\psi_i(0)+\phi_n(0)-\rho_n\zeta_i(\tau)/2-\pi/3] - e^{-\sqrt{3}\rho_n\zeta_i(0)/2}\cos[\psi_i(0)+\phi_n(0)-\rho_n\zeta_i(0)/2-\pi/3]$$
$$-\rho_n\tau e^{-\sqrt{3}\rho_n\zeta_i(0)/2}\cos[\psi_i(0)+\phi_n(0)-\rho_n\zeta_i(0)/2-\pi/6] + e^{\sqrt{3}\rho_n\zeta_i(\tau)/2}\cos[\psi_i(0)+\phi_n(0)-\rho_n\zeta_i(\tau)/2+\pi/3]$$
$$-e^{\sqrt{3}\rho_n\zeta_i(0)/2}\cos[\psi_i(0)+\phi_n(0)-\rho_n\zeta_i(0)/2+\pi/3] + \rho_n\tau e^{\sqrt{3}\rho_n\zeta_i(0)/2}\cos[\psi_i(0)+\phi_n(0)-\rho_n\zeta_i(0)/2+\pi/6] - \cos[\psi_i(0)$$
$$+\phi_n(0)+\rho_n\zeta_i(\tau)] + \cos[\psi_i(0)+\phi_n(0)+\rho_n\zeta_i(0)] - \rho_n\tau\cos[\psi_i(0)+\phi_n(0)+\rho_n\zeta_i(0)+\pi/2]\}, \quad (18)$$

where $\zeta_i(\tau)=\zeta_i(0)-\tau$ is used, which is valid as long as the electron energy change $\mu_i(\tau)$ is small and $d\zeta_i(\tau)/d\tau=-1$ holds. Equations (17) and (18) represent the phase space evolution of the ith electron during the second pass.

The field gain $da_n(\zeta)/d\tau$ caused by the electron microbunch in units of λ_r whose initial position is $\zeta_i(0)=\zeta+\tau$ is derived from substitution of $\psi_i(\tau)=\psi_i(0)+\Delta\psi_i(\tau)$ into Eq. (5) as follows:

$$\frac{da_n(\zeta)}{d\tau} = \frac{|a_n(0)|e^{i\phi_n(0)}}{3\rho_n^2}\{\exp(-\rho_n\zeta e^{i\pi/6})e^{i\pi/6}[1-\exp(-\rho_n\tau e^{i\pi/6})(1+\rho_n\tau e^{i\pi/6})] - \exp(\rho_n\zeta e^{-i\pi/6})e^{-i\pi/6}[1-\exp(\rho_n\tau e^{-i\pi/6})(1$$
$$-\rho_n\tau e^{-i\pi/6})] + \exp(-\rho_n\zeta e^{-i\pi/2})e^{-i\pi/2}[1-\exp(-\rho_n\tau e^{-i\pi/2})(1+\rho_n\tau e^{-i\pi/2})]\}, \quad (19)$$

when $|\Delta\psi_i(\tau)| \ll 1$.

The field $a_n(\zeta)$ is sequentially amplified from $\tau=0$ to $\tau=-\zeta$ by the electron microbunches whose initial position are $\zeta_i(0)=\zeta+\tau$ as it passes through the undulator. The field gain per pass is given by

$$\frac{da_n(\zeta)}{dn} = \int_0^{-\zeta}\frac{da_n(\zeta)}{d\tau}d\tau$$
$$= \frac{|a_n(0)|e^{i\phi_n(0)}}{3\rho_n^3}$$
$$\times\{-\rho_n\zeta[\exp(-\rho_n\zeta e^{i\pi/6})e^{i\pi/6} - \exp(\rho_n\zeta e^{-i\pi/6})e^{-i\pi/6}$$
$$+\exp(-\rho_n\zeta e^{-i\pi/2})e^{-i\pi/2}] - 2[\exp(-\rho_n\zeta e^{i\pi/6})$$
$$+\exp(\rho_n\zeta e^{-i\pi/6}) + \exp(-\rho_n\zeta e^{-i\pi/2})] + 6\}. \quad (20)$$

The leading slope of the output field for the second pass is thus given by

$$a_n(\zeta) + \frac{da_n(\zeta)}{dn} = \frac{|a_n(0)|e^{i\phi_n(0)}}{3\rho_n^3}$$
$$\times\{-\rho_n\zeta[\exp(-\rho_n\zeta e^{i\pi/6})e^{i\pi/6}$$
$$-\exp(\rho_n\zeta e^{-i\pi/6})e^{-i\pi/6}$$
$$+\exp(-\rho_n\zeta e^{-i\pi/2})e^{-i\pi/2}]$$
$$+(\rho_n^3-2)[\exp(-\rho_n\zeta e^{i\pi/6})$$
$$+\exp(\rho_n\zeta e^{-i\pi/6}) + \exp(-\rho_n\zeta e^{-i\pi/2})] + 6\}. \quad (21)$$

The amplitude and phase of the output field given by Eq. (21) are plotted as solid circles in Figs. 2(a) and 2(b), respectively, as a function of ζ. The solid line shows the output field of the second pass obtained in a time-dependent numerical calculation, which solves Eqs. (3)–(5) with an input field given by Eq. (15) with $\rho_n=1$ and represented by the dotted line. In the calculation, the shot-noise effect is neglected. One can see that the field given by Eq. (21) agrees well with the numerical calculation where $|\zeta|<3.5$ but the phase gradually deviates from the calculation where $|\zeta| \geq 3.5$. This is because the assumption that the field remains almost unchanged during the passage through an undulator

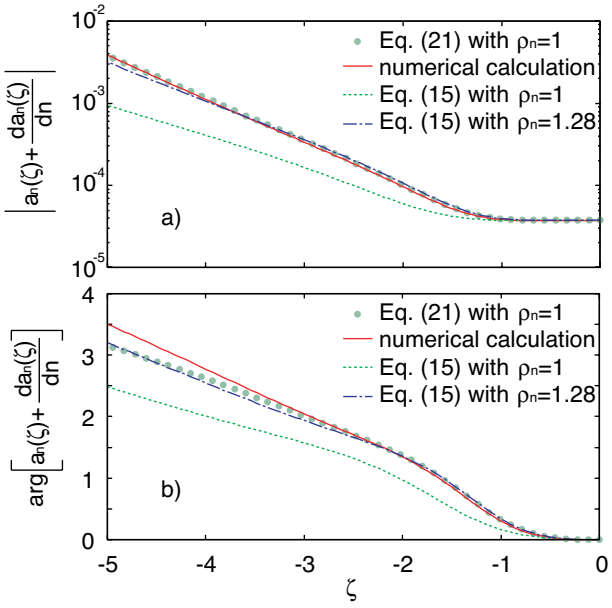

FIG. 2. (Color online) The amplitude (a) and phase (b) of the output field $a_n(\zeta)+da_n(\zeta)/d\zeta$ as a function of ζ. The solid circles stand for the output field of the second pass given by Eq. (21) with $\rho_n=1$, and the solid line is that obtained from a numerical calculation where Eq. (15) with $\rho_n=1$, which is represented by the dotted line, is used as an input field envelope. The dash-dotted line expresses an approximated output field of the second pass given by Eq. (15) with $\rho_n=1.28$. The amplitude of the front edge $|a_n(0)|=3.7\times10^{-5}$ is used.

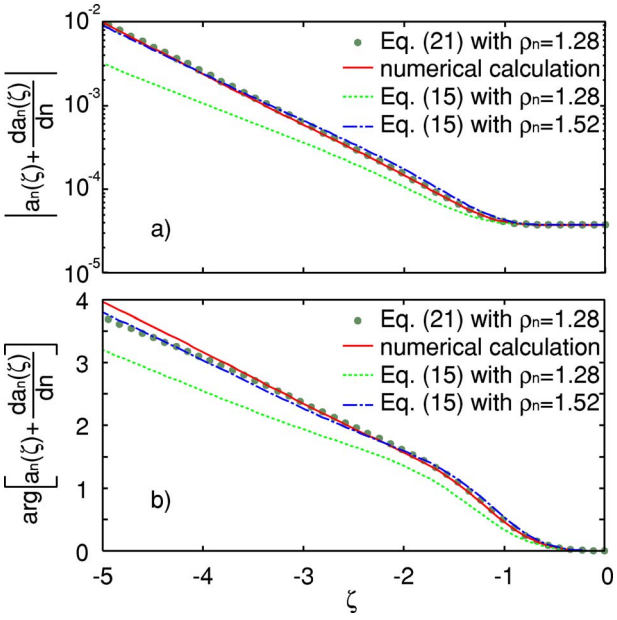

FIG. 3. (Color online) The amplitude (a) and phase (b) of the output field $a_n(\zeta)+da_n(\zeta)/d\zeta$ as a function of ζ. The solid circles stand for the output field of the third pass given by Eq. (21) with $\rho_n=1.28$, and the solid line is that obtained from a numerical calculation where Eq. (15) with $\rho_n=1.28$, which is represented by the dotted line, is used as an input field envelope. The dash-dotted line expresses an approximated output field of the third pass given by Eq. (15) with $\rho_n=1.52$. The amplitude of the front edge $|a_n(0)|=3.7\times10^{-5}$ is used.

no longer holds where $|\zeta|\geq3.5$ for the second pass. Nevertheless, the deviation does not affect significantly the evolution of the leading slope during the subsequent passes, since the position of the primary peak amplitude ζ_p shifts toward the front edge with pass number n and the field at large $|\zeta|$ stays behind the leading slope at saturation (see Fig. 1).

B. Optical field and electron phase space evolutions on pass numbers greater than 2

The output field of the second pass is equivalent to the input field for the third pass except for amplitude decrease due to the optical cavity loss α. If the input field for the third pass is found to be approximated by Eq. (15), the same procedure described in the previous subsection can be used for a study of the optical growth during the third pass. The dash-dotted line in Fig. 2 shows the field given by Eq. (15) with $\rho_n=1.28$. The amplitude of this field is different from that obtained in a numerical calculation (solid line) by only 10% to −20% where $|\zeta|<5$, and the phase is different from the numerical calculation by only ±0.17 rad. These results suggest that the input field for the third pass can be approximated by Eq. (15) with $\rho_3=1.28$.

The same procedure used for the second pass is thus employed to obtain the output field of the third pass. The solid circles in Fig. 3 represent the output field given by Eq. (21) when $\rho_3=1.28$. The solid line is the field obtained in a time-dependent numerical calculation where the input field is given by Eq. (15) with $\rho_3=1.28$ (dotted line) and shot-noise effects are neglected. One can see that the agreement between Eq. (21) and the numerical calculation for the third pass is better than that for the second pass. This is because the field gain decreases with increase of ρ_n as seen in Eq. (20), and the assumption that the field remains unchanged is valid over a wider range of ζ as ρ_n increases. The output field can be approximated by Eq. (15) with $\rho_4=1.52$, which is shown by a dash-dotted line in Fig. 3. In a similar way, one can obtain ρ_n of the input field for pass numbers greater than $n=4$ as well. For example $\rho_5=1.73$, $\rho_6=1.90$, and $\rho_7=2.05$.

As ρ_n increases, $\rho_n^3-2\sim\rho_n^3$ and Eq. (21) asymptotically approaches

$$a_n(\zeta)+\frac{da_n(\zeta)}{dn}\sim a_n(\zeta)+\frac{|a_n(0)|e^{i\phi_n(0)}}{3}\frac{1}{\rho_n^3}\times\{-\rho_n\zeta[\exp(-\rho_n\zeta e^{i\pi/6})e^{i\pi/6}-\exp(\rho_n\zeta e^{-i\pi/6})e^{-i\pi/6}+\exp(-\rho_n\zeta e^{-i\pi/2})e^{-i\pi/2}]\},\tag{22}$$

The field evolution per pass can also be obtained by differentiation of Eq. (15) with respect to the pass number n under the assumption that ρ_n is independent of ζ as follows:

$$\frac{da_n(\zeta)}{dn}=\frac{|a_n(0)|e^{i\phi_n(0)}}{3}\frac{d\rho_n}{dn}\{-\zeta[\exp(-\rho_n\zeta e^{i\pi/6})e^{i\pi/6}-\exp(\rho_n\zeta e^{-i\pi/6})e^{-i\pi/6}+\exp(-\rho_n\zeta e^{-i\pi/2})e^{-i\pi/2}]\}.\tag{23}$$

Equation (23) should be equal to Eq. (22) subtracted by $a_n(\zeta)$ as long as the gain is much higher than the optical cavity loss and ρ_n is large enough for Eq. (22) to hold. This yields

$$\frac{d\rho_n}{dn}=\frac{1}{\rho_n^2}.\tag{24}$$

When we assume that Eq. (22) holds when $\rho_n>2$, Eq. (24) gives

$$\rho_n\approx(3n-12)^{1/3}\tag{25}$$

for $n\geq7$. Substitution of Eq. (25) into Eq. (23) yields

$$\frac{1}{|a_n(\zeta)|}\frac{d|a_n(\zeta)|}{dn}\approx-(\sqrt{3}/2)\zeta(3n-12)^{-2/3},\tag{26}$$

when $\exp(-\sqrt{3}\rho_n\zeta/2)\gg1$. Equation (26) shows that the gain per pass decreases with increasing pass number n.

The parameter ρ_n can be derived from gradients of the FEL amplitude and phase with respect to ζ in the leading slope, which are obtained in a time-dependent numerical simulation. Figure 4 shows a simulation result at $\zeta=-2.8$ performed with the same parameter values as used in Fig. 1. The simulation values increase proportionally to Eq. (25) when $n\leq100$, and deviate gradually as the pass number increases for $n>100$. This deviation can be attributed to the effect of the optical cavity loss, which is neglected in the derivation of Eq. (25). The simulation results obtained at different ζ's are also similar to that at $\zeta=-2.8$.

The dependence of the gain on n represented by Eq. (26) agrees well with the simulation, as shown in Fig. 5. Once the

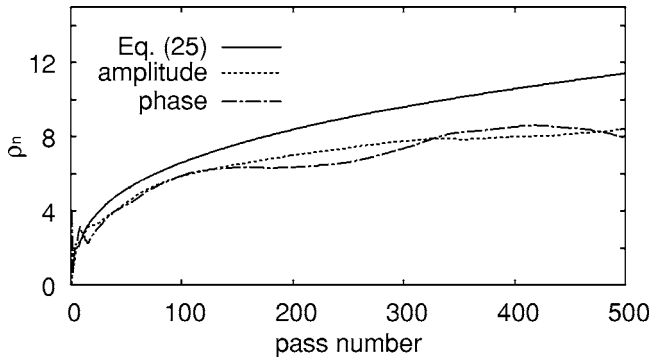

FIG. 4. The parameter ρ_n as a function of the pass number n. The solid line is Eq. (25). The dotted and dash-dotted lines are simulation results derived from gradients of optical amplitudes and phases, respectively, at $\zeta=-2.8$. The parameter values used in the simulation are the same as those in Fig. 1.

gain decreases down to the same level as the loss, the gain remains almost constant. The decrease of the gain with respect to n that is seen for small pass numbers is attributed to the increase of intensity gradient of the leading slope for the following reason. The field $a_n(\zeta)$ is amplified by interacting with the electron microbunches modulated by the preceding field $a_n(\zeta')$, where $\zeta'>\zeta$. The ratio of $|a_n(\zeta')|$ to $|a_n(\zeta)|$ decreases with increasing gradient of the amplitude. The gain at ζ therefore decreases with increase of ρ_n.

The discussion developed in the present section not only is based on the approximation that the output field of the nth pass is expressed by Eq. (15) with ρ_{n+1}, but also neglects the shot-noise effect. However, the agreement between the present analytical study and numerical simulations is excellent. This implies that the approximation is physically acceptable and the shot noise does not play a major role in the evolution of the leading slope. It is the ρ_n evolution of the leading slope that explains the field evolution of the FEL oscillation at $\delta L=0$.

C. Phase space evolution of electrons at $\delta L=0$

The time evolution of the electron distribution in a longitudinal phase space during interaction with the leading slope

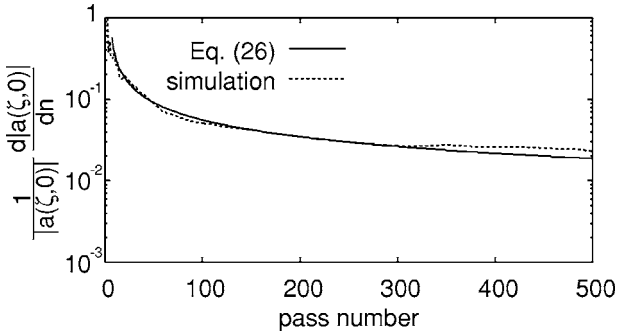

FIG. 5. Amplitude gain per pass as a function of the pass number n. The solid line is Eq. (26). The dotted line is the simulation result at $\zeta=-2.8$. The parameter values used in the simulation are the same as those in Fig. 1.

at $\delta L=0$ is similar to that in a SASE FEL, which is studied in our previous work [21]. We have shown that the longitudinal phase space composed of phase change $\Delta\psi_i(\tau)$ and energy change $\mu_i(\tau)$ is suitable to see the time evolution of the electron microbunching in a SASE FEL, especially in the early stage of evolution. In the present paper, the phase space used in Ref. [21] is employed and the electrons at $\tau=0$ are numbered depending on their longitudinal positions from the front to the rear. The relative position between two adjacent electrons is represented by $z_i(0)>z_{i+1}(0)$, and the relative phase is given by $\psi_i(0)>\psi_{i+1}(0)$ by definition. One can calculate the values of Eqs. (17) and (18) for each i and plot the point in the phase space of $\Delta\psi_i(\tau)$ and $\mu_i(\tau)$. The electrons within the resonant wavelength λ_r are distributed along an ellipse and are lined up along the ellipse counterclockwise as the identification number i increases. The electron distribution within λ_r at time instant τ in the longitudinal phase space of

$$\Delta\Psi_i(\tau)=\Delta\psi_i(\tau)\frac{3\rho_n^2}{|a_n(0)|e^{-\sqrt{3}\rho_n\zeta_i(\tau)/2}} \tag{27}$$

and

$$M_i(\tau)=\mu_i(\tau)\frac{3\rho_n}{|a_n(0)|e^{-\sqrt{3}\rho_n\zeta_i(\tau)/2}} \tag{28}$$

is shown in Fig. 6 for various initial positions. In the calculation of Eqs. (27) and (28) for each $\zeta_i(0)$, Eqs. (18) and (17) are used, respectively. The shape of the distribution gradually changes when $\rho_n\tau<4$ and remains almost constant when $\rho_n\tau\geq 4$. This threshold value $\rho_n\tau=4$ is quite similar to that of a SASE FEL [21]. The difference of the phase space evolution at $\delta L=0$ from that of the SASE is that the evolution depends on the initial position of the electron microbunch when $\rho_n\tau<4$ and $|\rho_n\zeta_i(0)|<4$, as shown in Fig. 6. The phase space evolutions are similar to each other where $|\rho_n\zeta_i(0)|\geq 4$.

In the following, the field and electron phase space evolutions are studied in the high-gain regime, which is defined by $\rho_n\tau\geq 4$ in the present paper. In the high-gain regime, the exponentially growing terms only survive in Eqs. (15), (17), and (18), and the field is given by

$$a_n(\zeta)\sim\frac{|a_n(0)|}{3}\exp[-\sqrt{3}\rho_n\zeta/2+i\phi_n(\zeta)], \tag{29}$$

where $\phi_n(\zeta)=-\rho_n\zeta/2+\phi_n(0)$. The energy and phase of the ith electron are respectively given by

$$\mu_i(\tau)\sim\frac{2|a_n(0)|e^{-\sqrt{3}\rho_n\zeta_i(\tau)/2}}{3\rho_n}\cos\{\psi_i(0)+\phi_n[\zeta_i(\tau)]-\pi/6\}, \tag{30}$$

$$\Delta\psi_i(\tau)\sim\frac{2|a_n(0)|e^{-\sqrt{3}\rho_n\zeta_i(\tau)/2}}{3\rho_n^2}\cos\{\psi_i(0)+\phi_n[\zeta_i(\tau)]-\pi/3\}. \tag{31}$$

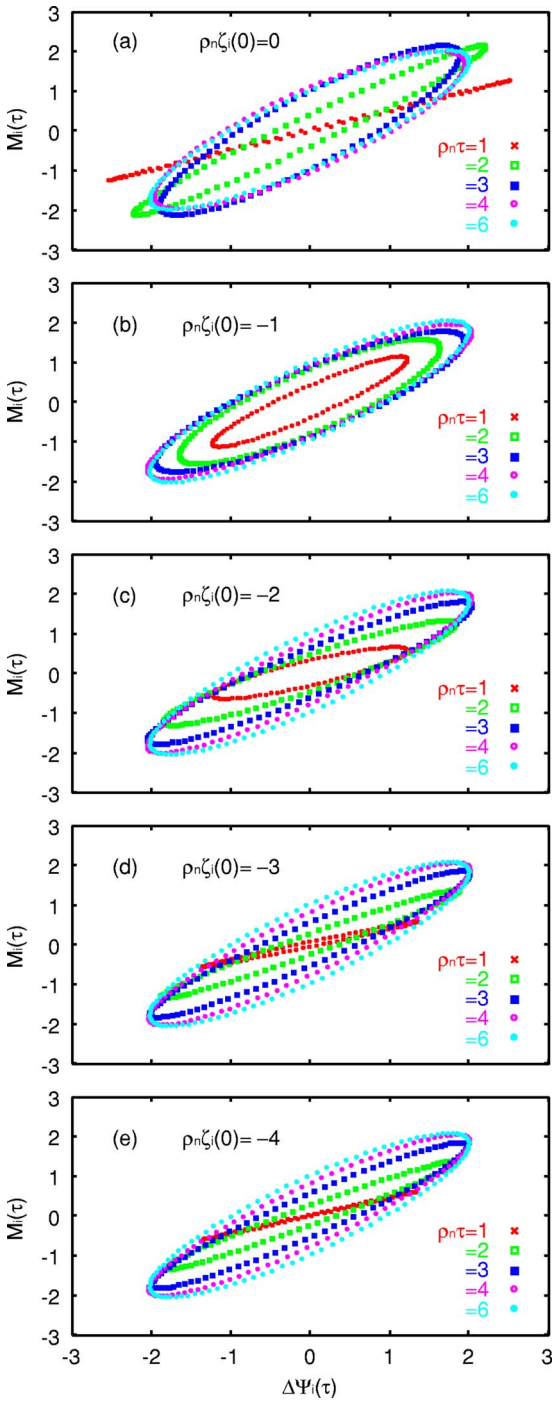

FIG. 6. (Color online) Electron distributions in a normalized phase plane of $\Delta\Psi_i(\tau)$ given by Eq. (27) and $M_i(\tau)$ given by Eq. (28) for various initial positions $\rho_n\zeta_i(0)$'s when $\rho_n\tau=1,2,3,4,6$. The electrons are asymptotically distributed along an ellipse expressed by $\Delta\Psi_i(\tau)^2+M_i(\tau)^2-\sqrt{3}\Delta\Psi_i(\tau)M_i(\tau)=1$. The center of the electron microbunch is asymptotically located at $[\Delta\Psi_i(\tau),M_i(\tau)]=(0,-1)$.

The longitudinal phase space composed of $\Delta\Psi_i(\tau)$ and $M_i(\tau)$ is simply represented by the ellipse $\Delta\Psi_i(\tau)^2+M_i(\tau)^2-\sqrt{3}\Delta\Psi_i(\tau)M_i(\tau)=1$. The ellipse rotates clockwise as $\phi_n[\zeta_i(\tau)]$ increases linearly with τ, while its size remains constant. This shows that the electron microbunching develops exponentially in size with the FEL amplitude and the position of the microbunch center shifts linearly with the FEL phase.

The center of the microbunch is the place where electrons within the resonant wavelength λ_r are concentrated. The electron at the microbunch center, satisfies the condition of $\Delta\psi_c(\tau)=0$, since $\Delta\psi_i(\tau)=-\Delta\psi_j(\tau)$ when $\psi_i(0)=\psi_c(0)+\delta\theta$ and $\psi_j(0)=\psi_c(0)-\delta\theta$ from Eq. (18). The $(c-1)$th electron, which is located just in front of the microbunch center, satisfies the condition of $\Delta\psi_{c-1}(\tau)<0$, and the $(c+1)$th electron satisfies $\Delta\psi_{c+1}(\tau)>0$. The intersection of the ellipse and the line $\Delta\psi_i(\tau)=0$ where $\mu_i(\tau)<0$ is the location of the microbunch center. Thus the microbunch center in the high-gain regime is located at $[\Delta\Psi_i(\tau),M_i(\tau)]=(0,-1)$ in Fig. 6 and the electrons inside the microbunch are concentrated around $\psi_i(0)+\phi_n[\zeta_i(\tau)]-\pi/3=\pi/2$ when $\rho_n\tau\geq 4$. The phase of the microbunch center is $\pi/6$ ahead of a resonant electron every resonant FEL wavelength. This phase relation is similar to that in a low-gain FEL where an electron beam above resonance is injected, explaining the positive FEL gain. In the longitudinal phase space of $\Delta\psi_i(\tau)$ and $\mu_i(\tau)$, the size of the ellipse expands exponentially with time due to the exponential increase of $|a_n[\zeta_i(\tau)]|$, while that in a SASE FEL expands with increase of $a(\tau)$. The exponential decrease of the energy of the microbunch center corresponds to the exponential decrease of the energy of the microbunch as a whole. The energy radiated by the microbunch is used for field amplification.

This phase space evolution in the high-gain regime is quite similar to that in a SASE FEL [21], but there is a noticeable difference between them. The electron microbunches lose almost the same amount of their energy at the same position in a frame moving at the speed of light but at different times in the FEL oscillations at $\delta L=0$, while the electron microbunches operating in a SASE FEL lose almost the same amount of their energy at the same time but different positions.

VI. SATURATION

A. The optimum bunching

When optimum microbunching occurs, the electron microbunch generates the maximum amount of radiation and amplifies the optical pulse most strongly. This optimum bunching is thus closely related to the primary peak amplitude of the optical pulse. Insertion of Eq. (31) into Eq. (5) gives the amplitude gain at time τ:

$$\frac{d|a_n(\zeta)|}{d\tau}=-\left\langle \cos\left(\psi_i(0)+\phi_n(\zeta)+\frac{2|a_n(\zeta)|}{\rho_n^2}\cos[\psi_i(0)+\phi_n(\zeta)-\pi/3]\right)\right\rangle_{\zeta_i(\tau)=\zeta}, \tag{32}$$

where $a(\zeta,\tau)\approx a(\zeta,0)=a_n(\zeta)$ due to the small gain at $\delta L=0$. The amplitude gain calculated as a function of $|a_n(\zeta)|/\rho_n^2$ is denoted by a solid curve in Fig. 7. In the calculation, the value of $\psi_i(0)+\phi_n(\zeta)$ is uniform over 2π. When

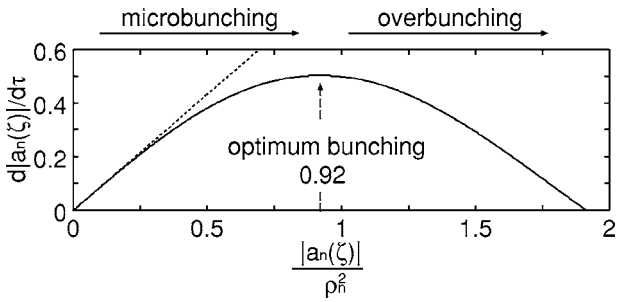

FIG. 7. The amplitude gain at time τ, $d|a_n(\zeta)|/d\tau$, as a function of $|a_n(\zeta)|/\rho_n^2$ given by Eq. (32) (solid curve). The dotted line is derived from Eq. (19) when $|a_n(\zeta)|/\rho_n^2 \ll 1$.

$|a_n(\zeta)|/\rho_n^2 \ll 1$, the amplitude gain is also derived from Eq. (19), which is denoted by a dotted line in Fig. 7. The amplitude gain begins to deviate from the dotted line around $|a_n(\zeta)|/\rho_n^2=0.4$ and reaches the maximum value of 0.5 at $|a_n(\zeta)|/\rho_n^2=0.92$. The maximum value is confirmed by the simulation shown in Fig. 8, which displays a contour plot of the intensity gain $\partial|a(\zeta,\tau)|^2/\partial\tau$ as functions of ζ (x axis) and τ (y axis) and shows $\partial|a(\zeta,\tau)|^2/\partial\tau=2|a(\zeta,\tau)|\partial|a(\zeta,\tau)|/\partial\tau \approx |a(\zeta,0)|$ around $\zeta=\zeta_p$. After the optimum bunching, the gain begins to decrease because of the overbunching as in a SASE FEL [24].

The primary peak amplitude of the optical pulse is thus given by

$$|a_n(\zeta_p)| = \frac{|a_n(0)|}{3} e^{-\sqrt{3}\rho_n\zeta_p/2} = 0.92\rho_n^2, \tag{33}$$

which is 80% of $1.2\rho_n^2$, the peak amplitude of the SASE with FEL parameter $\rho_n\rho$ in the steady-state regime [10]. The pulse length during which the intensity $|a_n(\zeta)|^2$ rises from 10% to 90% of the primary peak is given by

$$\frac{\ln 9}{\sqrt{3}\rho_n} = \frac{1.27}{\rho_n} \tag{34}$$

in units of L_c. The synchrotron oscillation of electrons caused by the overbunching leads to formation of subsequent peaks

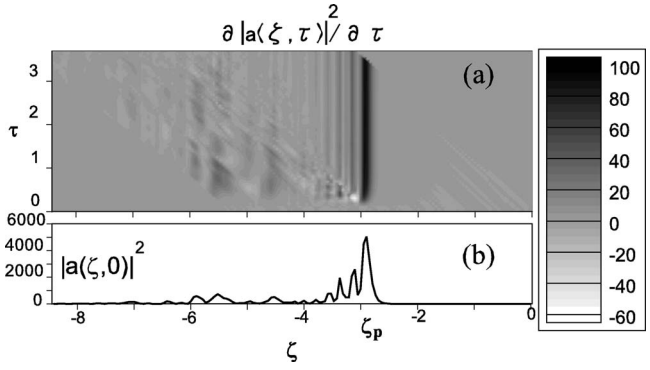

FIG. 8. A contour plot of the intensity gain $\partial|a(\zeta,\tau)|^2/\partial\tau$ as functions of ζ (x axis) and τ (y axis) on the 1000th pass (a) and the corresponding optical intensity profile $|a(\zeta,0)|^2$ plotted in linear scale (b). The parameters used in the simulation are the same as those used in Fig. 1.

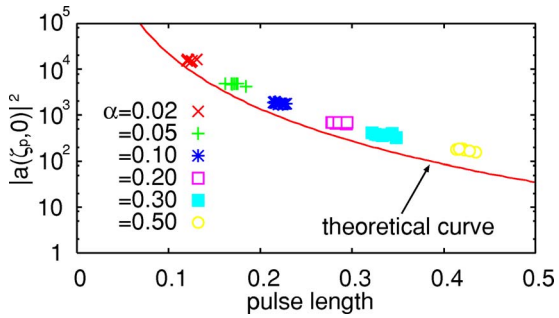

FIG. 9. (Color online) Semilogarithmic plot of the primary peak intensity $|a(\zeta_p,0)|^2$ as a function of the pulse length, during which the intensity rises from 10% to 90% of the peak. The points are time-dependent numerical simulation results. The solid line is the theoretical curve obtained from Eqs. (33) and (34).

where $\zeta<\zeta_p$. The intensities of such secondary peaks are lower than half that of the primary peak [14]. Thus the full width at half maximum (FWHM) pulse length is nearly equal to the value of Eq. (34). Figure 9 shows the primary peak intensity as a function of the FWHM pulse length in units of L_c in saturation. The theoretical curve given by Eq. (33) as a function of the corresponding value of Eq. (34) qualitatively agrees with time-dependent simulation values denoted as points for many different parameter sets of ρ and α, though the absolute value of the theoretical curve is somewhat different from the simulations. The difference can be attributed to the estimation of the pulse length of Eq. (34), in which the field is approximated by Eq. (15) even near ζ_p. The amplitude profile near ζ_p should be represented by a more realistic pulse shape like a hyperbolic secant pulse. In this case, the pulse length becomes 1.15 times longer than that given by Eq. (34), which leads to better agreement between the simulation values and the present theoretical curve.

B. The primary peak field at saturation

The gain per pass decreases almost linearly with decreasing $|\zeta|$, as seen in Eq. (20). This means the evolution of ρ_n at smaller $|\zeta|$ stops on the smaller pass number when the gain decreases down to the level of the optical cavity loss α. The optical field reaches saturation when the gain at ζ_p becomes as small as α, and a self-similar pulse is generated every pass, as shown in Ref. [14], establishing the sustained FEL oscillation at $\delta L=0$ and resulting in disappearance of the lethargy effect. Thus ρ_n at saturation, which is defined by ρ_s in the present paper, should depend on ζ and increase with increasing $|\zeta|$. This is supported by the temporal profile of the optical pulse at saturation depicted in Fig. 1, which shows a slight increase of the exponent of the field function on the leading slope with increase of $|\zeta|$. It might, however, be useful to estimate $\rho_s(\zeta)$ near the position of the peak amplitude ζ_p under the assumptions that $\rho_s(\zeta)$ has a constant value independent of ζ and that the amplitude gain at the peak is equal to $\alpha/2$ in saturation. These assumptions together with Eq. (20) result in

$$\frac{1}{|a_n(\zeta_p)|}\frac{d|a_n(\zeta)|}{dn} \approx \frac{1}{\rho_s^3}\left(-\frac{\sqrt{3}\rho_s\zeta_p}{2}-2\right)=\frac{\alpha}{2}, \tag{35}$$

since Eq. (20) asymptotically approaches $da_n(\zeta)/dn \sim a_n(\zeta) \times(-\rho_n\zeta e^{-i\pi/6}-2)/\rho_n^3$ when $|\rho_n\zeta|>4$. Substitution of Eq. (35) into Eq. (33) yields

$$\frac{|a_n(0)|}{3}\exp\left(\frac{\rho_s^3\alpha}{2}+2\right)=0.92\rho_s^2. \tag{36}$$

The parameter ρ_s is represented as a function of α, as described in the following paragraph when $|a_n(0)|$ is derived.

In the front portion of the leading slope where the single-pass gain $\frac{1}{|a_n(\zeta)|^2}\frac{d|a_n(\zeta)|^2}{dn}$ is smaller than α, the field $a_n(0)$ is a random superposition of spontaneous radiation emitted over n passes and is given by $|a_n(0)|=|a(0)|\sqrt{n}$ for the pass number $n<1/\alpha$ and $|a_n(0)|=|a(0)|/\sqrt{\alpha}$ for $n\geq 1/\alpha$. Here $|a(0)|$ is equivalent to the amplitude of spontaneous radiation for a single pass emitted in about one gain length [24] and is estimated to be $|a(0)|=\sqrt{2\pi\rho/N_e}$ from Eq. (5), since the variance of $\langle\cos[\psi_i(\tau)]\rangle_{\zeta_i(\tau)=\zeta}$ per the cooperation length is given by $(4\pi\rho)/(2N_e)$ from a statistical consideration [23]. Here $N_e=n_e\lambda_r\Sigma$ is the number of electrons contained in a unit volume of $\lambda_r\Sigma$. The electron beam density is given by $n_e=(16\rho^3\gamma_0^3\varepsilon_0 mc^2k_w^2)/(e^2a_w^2F^2)$ from Eq. (1), and thus

$$N_e=(4\pi\rho)^3\frac{\lambda_r\varepsilon_0\Sigma\gamma_0^3mc^2}{\pi e^2a_w^2\lambda_w^2F^2}. \tag{37}$$

Substitution of Eq. (37) into $|a(0)|=\sqrt{2\pi\rho/N_e}$ gives

$$|a(0)|=\frac{1}{\rho}\frac{e}{\sqrt{32\pi mc^2\varepsilon_0}}\frac{Fa_w\lambda_w}{\sqrt{\gamma_0^3\Sigma\lambda_r}}. \tag{38}$$

The effective radiation area is $\Sigma=\lambda_rZ_R/2$ where $Z_R=R\lambda_w/(4\pi\rho)$ is the Rayleigh range and $R\geq 1$ for 1D SASE FEL theory [24]. Substitution of $\Sigma=R\lambda_w\lambda_r/(8\pi\rho)$ into Eq. (38) yields $|a(0)|=P/\sqrt{\rho R}$, where

$$P=\frac{e}{\sqrt{mc^2\varepsilon_0}}\sqrt{\frac{F^2a_w^2\gamma_0}{\lambda_w(1+a_w^2)^2}}. \tag{39}$$

The parameter P ranges from 1×10^{-6} to 2×10^{-5} for almost all the Compton FELs [26], ρ ranges from 0.001 to 0.01, and R is of the order of unity. The amplitude at $\zeta=0$ when $n\geq 1/\alpha$ is given by

$$|a_n(0)|=P/\sqrt{\alpha\rho R}. \tag{40}$$

Insertion of Eq. (40) into Eq. (36) gives

$$\rho_s^3\alpha=\ln(\alpha\rho R)-2\ln P+4\ln(\rho_s)-1.97. \tag{41}$$

Parameters such as a_w, λ_w, and γ_0 used in the simulation shown in Fig. 1 yield $P=2.5\times10^{-6}$. Substitution of this value of P into Eq. (41) gives ρ_s as a function of $\alpha^{-1/3}$ represented by the solid curve in Fig. 10. The dashed curve in Fig. 10 stands for ρ_s when $\rho=0.01$ and $P=1.0\times10^{-6}$ and the dash-dotted curve when $\rho=0.001$ and $P=2.0\times10^{-5}$. The curve ρ_s as a function of $\alpha^{-1/3}$ falls in the area surrounded between the dashed and dash-dotted lines when ρ varies from

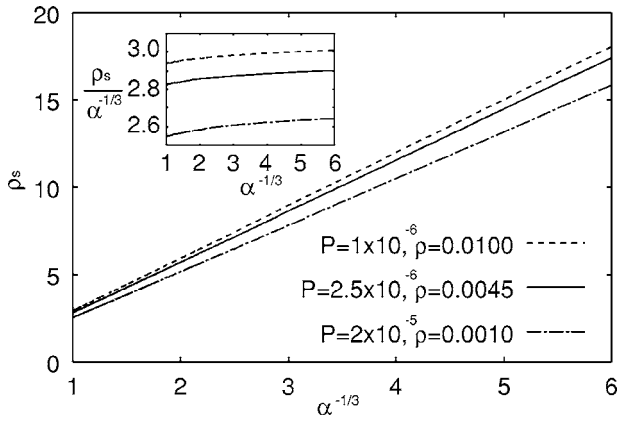

FIG. 10. The characteristic parameter ρ_s at saturation as a function of $\alpha^{-1/3}$. The solid line shows ρ_s derived from Eq. (41) when $P=2.5\times10^{-6}$ and $\rho=0.0045$, the dashed line when $P=1\times10^{-6}$ and $\rho=0.01$, and the dash-dotted line when $P=2\times10^{-5}$ and $\rho=0.001$. The ratio of ρ_s to $\alpha^{-1/3}$ depends on the FEL, but the difference is small among existing FELs. The inset shows $\rho_s/\alpha^{-1/3}$ as a function of $\alpha^{-1/3}$.

0.001 to 0.01 and P ranges from 1×10^{-6} to 2×10^{-5}. From the figure, ρ_s is approximately given by

$$\rho_s\approx 2.8\alpha^{-1/3}. \tag{42}$$

Equation (42) can be applied to almost all Compton FELs [26]. The variations of P and ρ causes uncertainty of ±10% for the coefficient 2.8 in Eq. (42).

The position of the primary peak at saturation is derived from Eqs. (35) and (42):

$$\zeta_p\approx -15/\rho_s\approx -5.4\alpha^{1/3}. \tag{43}$$

These values of 15 and 5.4 in Eq. (43) have uncertainty of ±20% due to the variations of P and ρ. The gain per pass given by Eq. (20) can be used where $|\zeta|$ is shorter than L_b, L_s, and $|\zeta_p|$. Thus both L_b and L_s are required to be longer than $15/\rho_s$ in order for Eqs. (33), (34), and (42) to hold. The requirement on $L_s=4\pi\rho N_w$ corresponds to $j_0>310\alpha$. The field evolution in the leading slope where $|\zeta|<|\zeta_p|$ does not depend on L_b or L_s, as long as both L_b and L_s are longer than $|\zeta_p|$. The evolution of the leading slope shown in Fig. 1 should thus appear even when $L_b\gg|\zeta_p|$, $L_s\gg|\zeta_p|$ or saturation in SASE mode occurs within the first single pass: $\rho N_w>1$.

C. Efficiency

The energy carried by the intracavity radiation over unit length of λ_r along the propagation direction is given from Eq. (2) by

$$\varepsilon_0\lambda_r\Sigma E(\zeta,\tau)^2=\frac{\varepsilon_0\lambda_r\Sigma\gamma_0^4m^2c^4|a(\zeta,\tau)|^2(4\pi\rho)^4}{4\pi^2e^2a_w^2\lambda_w^2F^2}. \tag{44}$$

The time derivative of the intracavity energy, $\partial[\varepsilon_0\lambda_r\Sigma E(\zeta,\tau)^2]/\partial\tau$, is equal to the amount of the instantaneous energy loss of the microbunch given by $-N_emc^2d\langle\gamma_i(\tau)-\gamma_0\rangle_{\zeta_i(\tau)=\zeta}/d\tau$. The average of the instanta-

neous energy loss of the microbunch at time τ is thus given by

$$-\frac{d\langle\mu_i(\tau)\rangle_{\zeta_i(\tau)=\zeta}}{d\tau}=\frac{\partial|a(\zeta,\tau)|^2}{\partial\tau}. \tag{45}$$

Here Eq. (37) is used in the derivation of Eq. (45).

The energy loss of the microbunch at time τ is asymptotically equal to $-d\langle\mu_i(\tau)\rangle_{\zeta_i(\tau)=\zeta}/d\tau\sim\sqrt{3}|a_n(\zeta)|^2/\rho_n^2$, as derived from Eqs. (45), (15), and (19). Here $a(\zeta,\tau)\approx a(\zeta,0)=a_n(\zeta)$ is used. The microbunch mainly loses its energy around the position of the primary peak (see Fig. 8). The instantaneous energy loss of the microbunch at the primary peak in saturation is given by $\sqrt{3}|a_n(\zeta_p)|^2/\rho_s^2\approx 11.5\alpha^{-2/3}$ from Eqs. (33) and (42) and is estimated to be 85 when $\alpha=0.05$. This value of the instantaneous energy loss agrees well with the simulation result shown in Fig. 8. The energy loss of the electron microbunch during interaction with the leading slope is almost equal to $\sqrt{3}|a_n(\zeta_p)|^2/\rho_n^2$ multiplied by the optical pulse length represented by Eq. (34), where $|a_n(\zeta_p)|$ is given by Eq. (33). The extraction efficiency of the microbunch at ζ_p, $\eta=-\rho\langle\mu_i(\tau_p)\rangle_{\zeta_i(\tau_p)=\zeta}$, is thus approximated by

$$\eta\approx 1.9\rho_n\rho, \tag{46}$$

where τ_p is the time that the microbunch slips back to ζ_p. Equation (46) yields $\eta=0.065$ at saturation when $\rho=0.0045$ and $\alpha=0.05$. This efficiency is consistent with the value obtained in the simulation shown in Fig. 8.

VII. DISCUSSION

A. Sequential emission of intense radiation

The radiation from the whole electron bunch at time τ, $-d\langle\mu_i(\tau)\rangle_{\zeta_i(\tau)=\zeta}/d\tau=\partial|a(\zeta,\tau)|^2/\partial\tau$, has an intensity profile similar to that of the optical pulse overlapped by the electron bunch, $|a_n[\zeta_i(\tau)]|^2$, as shown in Eq. (19). The optical intensity at ζ continues to build up until the electron bunch escapes from ζ due to the slippage. The intensity gain per pass at ζ, $d|a_n(\zeta)|^2/dn$, is almost proportional to the intensity itself $|a_n(\zeta)|^2$ multiplied by the overlapping time $|\zeta|$, as shown in Eq. (20). The intensity gain is thus highest at ζ_p. The buildup in intensity is reproduced in a time-dependent simulation shown in Fig. 8, which displays a contour plot of the intensity gain $\partial|a(\zeta,\tau)|^2/\partial\tau=-d\langle\mu_i(\tau)\rangle_{\zeta_i(\tau)=\zeta}/d\tau$ as functions of τ and ζ. The gain is highest around ζ_p and is almost constant during the overlapping time. The oscillatory behavior of the radiation intensity seen in the range $|\zeta|>|\zeta_p|$ indicates that optimum bunching is established at ζ_p and then overbunching occurs. In FELs at $\delta L<0$, electrons radiate their energies in a similar way to those that are initially located at $|\zeta_i(0)|\geq|\zeta_p|$ in FELs at $\delta L=0$, since those electrons interact only with fields much stronger than the spontaneous emission level at saturation due to the optical cavity feedback.

B. Comparison with numerical simulations

Substitution of Eq. (42) into Eqs. (33) and (34) gives the peak intracavity intensity $|a_s(\zeta_p)|^2$ and the pulse length at saturation, respectively, as follows:

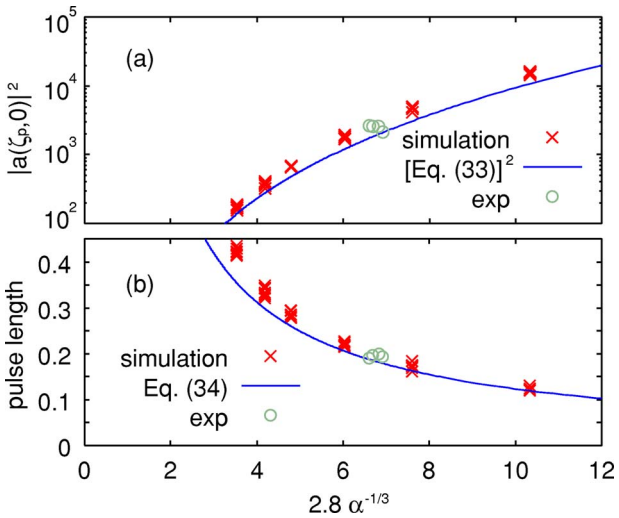

FIG. 11. (Color online) Semilogarithmic plot of the primary peak intensity $|a(\zeta_p,0)|^2$ as a function of $2.8\alpha^{-1/3}$ (a) and linear plot of the optical pulse length (b) during which the intensity rises from 10% to 90% of the peak as a function of $2.8\alpha^{-1/3}$. The crosses are simulation values. The open circles are experimental data obtained at the JAERI FEL. The solid line in (a) is the square of Eq. (33) and that in (b) is Eq. (34), where ρ_s derived from Eq. (41), $P=2.5\times10^{-6}$, and $\rho=0.0045$ is substituted into ρ_n in Eqs. (33) and (34).

$$|a_s(\zeta_p)|^2\approx 52\alpha^{-4/3}, \tag{47}$$

$$\ln 9/(\sqrt{3}\rho_s)\approx 0.45\alpha^{1/3}. \tag{48}$$

The peak intracavity intensity in saturation reaches approximately $37\alpha^{-4/3}$ times higher than that a long-pulse SASE FEL with the same ρ can reach in the steady-state regime. The corresponding peak intensity coupled out of the optical cavity is given by $\alpha|a_s(\zeta_p)|^2=52\alpha^{-1/3}$ in the ideal case where the output coupling loss is equal to the total cavity loss α. The peak amplitude of the intracavity radiation given by $E(\zeta_p,\tau)$ is proportional to $(\rho/\alpha^{1/3})^2$, as derived from Eqs. (44) and (47). The pulse length is represented by $0.036(\rho/\alpha^{1/3})^{-1}$ in units of the wavelength λ_r. The peak amplitude and the pulse length at saturation are thus found to scale with the electron beam density and optical cavity loss. In order to test these scalings, we performed numerical simulations similar to our previous work [14]. Both L_b and L_s used in those simulations are longer than the distance from $\zeta=0$ to ζ_p at saturation. The simulations were made with many combinations of ρ between 0.002 and 0.014 and α between 0.02 and 0.50. The peak intensity and the number of cycles of the FEL pulse length averaged from the 1000th to 2000th pass are denoted by crosses as a function of $2.8\alpha^{-1/3}$ in Fig. 11. The simulation values agree well with the theoretical curves given by Eqs. (47) and (48).

Figure 12(a) shows ρ_s as a function of $2.8\alpha^{-1/3}$. The solid curve representing Eq. (42) is almost equal to simulation values denoted by crosses, which are obtained from gradients of amplitudes and phases at the position where $|a(\zeta,0)|=|a(\zeta_p,0)|/3$ and averaged from the 1000th to the 2000th pass. However, ρ_s obtained at other positions gradually ap-

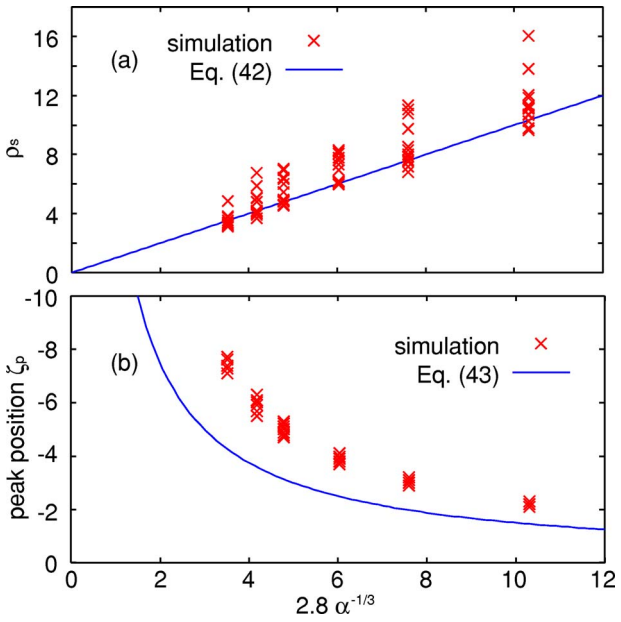

FIG. 12. (Color online) The characteristic parameter ρ_s (a) and the position of the primary peak ζ_p (b) at saturation as a function of $2.8\alpha^{-1/3}$. The simulation values are denoted by crosses. Those in (a) are derived from gradients at positions where the amplitude is one-third of the peak amplitude. The solid line in (a) shows Eq. (42) and that in (b) shows Eq. (43).

proaches zero as ζ goes toward the front edge $\zeta=0$.

Figure 12(b) shows the position of the principal peak ζ_p as a function of $2.8\alpha^{-1/3}$. The crosses denote simulation values, and the solid curve represents Eq. (43). The shape of the solid curve is similar to that formed by simulation values, though their absolute values are different from each other. The disagreement of ζ_p between Eq. (43) and the simulations comes from the facts that Eq. (15) does not represent the optical field at saturation in an exact sense and ρ_s depends on ζ as mentioned in Sec. VI. The same facts account for the systematic deviation of ρ_s from Eq. (42) as ζ goes toward the front edge, which was mentioned in the previous paragraph. Equation (15) can, however, represent the field of the leading slope during the evolution rather exactly.

C. Comparison with experimental results

A comparison with JAERI FEL experiments was performed. The optical pulse lengths measured were 250 fs FWHM independently of the wavelength, which varies from 22 to 18 μm as a_w is varied from 0.7 to 0.4 [13]. The extraction efficiency from electrons to FEL varied from 6.0% to 3.4% depending on a_w, while the energy of the incident electron bunch was 8.4 mJ [12]. The cavity loss α was approximately 7%. Our simulation with JAERI FEL parameters shows that approximately 2/3 of the total energy of the optical pulse is carried by the primary peak area at saturation [14]. The intensities of the primary peaks obtained after the area correction are denoted by solid circles in Fig. 11(a), and FWHM pulse lengths are denoted by solid circles in Fig. 11(b). Both of them agree with the present theoretical curves well.

The present scaling can be applied to many Compton FELs. For example, the intracavity intensity is estimated from Eqs. (47) and (48) to be $|a(\zeta_p)|^2=1.8\times10^3$ with duration of 0.19 FWHM in units of L_c when $\alpha=0.07$, which is typical at the JAERI FEL at $\lambda_r=22$ μm [12]. The intracavity peak intensity is 1280 times higher than 1.4, which is what a long-pulse SASE FEL with the same ρ can reach in the steady-state regime [10], and the peak intensity coupled out of the optical cavity is 90 times higher than that of the SASE FEL when the coupling loss is the same as the total cavity loss. The optical pulse length is given by $0.015/\rho$ in units of the wavelength λ_r. One can thus produce intense optical pulses with a few wavelength cycles by using the FEL oscillations at $\delta L=0$ when ρ is greater than 0.004.

D. Transient evolution at $\delta L=0$

In the front portion of the leading slope where the single-pass gain for a uniform input field is smaller than α, the field is affected by shot noise every pass even after saturation as seen in Fig. 1. The range affected by shot noise is estimated as $|\zeta|\leq1$ [24]. The field affected by shot noise in turn affects the subsequent amplified field every pass, and results in a random slight shift of the leading slope along the propagation direction. This behavior is responsible for the peak position fluctuation or the efficiency variation observed in a time-dependent simulation [14].

The dissipation of oscillation at $\delta L=0$ after many passes, which is shown in Refs. [6,7], can be reproduced by removing the shot noise of electrons except for the first pass. The optical field intensity at $|\zeta|\leq1$, where the field is sustained by the shot noise, decreases exponentially with respect to n due to the cavity loss α, while the field at $|\zeta|\geq1$ evolves with n when the gain is much higher than the cavity loss. The characteristic parameter of the field ρ_n and the peak intensity can almost reach the values given by Eqs. (42) and (47), respectively, but after that the intensity of the leading slope continues to decrease and finally dissipates. This is because the intensity at $|\zeta|\leq1$ decreases exponentially while the characteristic parameter ρ_n remains close to the value given by Eq. (42). In real physical situations, however, the intensity at $|\zeta|\leq1$ is kept at around the level given by Eq. (40), and the FEL oscillation at $\delta L=0$ is sustained. This is the reason why the small shot-noise of an electron bunch must be included in a numerical simulation to reproduce the lasing at $\delta L=0$ [14].

E. Evolution of the peak amplitude at $\delta L=0$

The evolution of the peak optical amplitude is found to scale with $n^{2/3}$ from Eqs. (33) and (25), when both L_b and L_s are larger than 15 in units of L_c. This evolution is different from the superradiant evolution $|a(\zeta_p)|\propto n$, which is presented in the analytical study [7] or the numerical study [17] for a short-pulse FEL oscillator at $\delta L=0$. Our numerical simulation supports both types of peak amplitude evolution. The peak amplitude scales with $n^{2/3}$ when both L_b and L_s are longer than 15. The index of the scaling function approaches unity as L_b or L_s becomes shorter than 15. The peak ampli-

tude evolution thus strongly depends on the lengths of L_b and L_s.

The present analytical study as well as our time-dependent numerical simulation show that the evolution of the exponent of the field function on the leading slope, ρ_n, characterizes the FEL dynamics at $\delta L=0$. The characteristic parameter ρ_n at the position ζ scales with $n^{1/3}$ as seen in Eq. (25), when both L_b and L_s are longer than $|\zeta|$. The evolution of the optical field where $|\zeta| \leq 15/\rho_s$ does not depend on how the field evolves where $|\zeta| > 15/\rho_s$, although the peak amplitude is formed where $|\zeta| > 15/\rho_s$ before saturation. The evolution of ρ_n in the leading slope where $|\zeta| \leq 15/\rho_s$ is therefore not related to the peak amplitude evolution, which shows the superradiant behavior only when L_s or L_b is much shorter than 15.

F. Sideband instability at $\delta L=0$

Sideband instability has been attributed to the lasing at $\delta L=0$ in Ref. [16], but such instability is also observed in FELs where $\delta L<0$ [27]. Unfortunately, a clear explanation has not been given to the difference between the instability at $\delta L=0$ and that where $\delta L<0$ in Ref. [16]. The present study shows that the exponent of the slowly varying envelope of the field on the leading slope at $\delta L=0$ is $-\rho_n \zeta e^{i\pi/6}$ where $\rho_n|\zeta| \geq 4$, as seen in Eq. (15), and that of the carrier wave is $i(k_r z-\omega_r t)=i\zeta/(2\rho)$. The wave number of the field on the leading slope is therefore $(1-\rho_n \rho)k_r$, indicating that the mean wavelength shifts to a longer wavelength with each increment of n. The wavelength shift can qualitatively explain generation of sidebands at $\delta L=0$.

VIII. CONCLUSION

In this paper we have presented an analytical description of the FEL oscillation at $\delta L=0$ from startup to saturation. It has been shown that the evolution of the leading slope of the FEL pulse plays a crucial role in generating intense few-cycle optical pulses at $\delta L=0$. The phase space evolution of electrons at $\delta L=0$ during interaction with the leading slope of the FEL pulse is solved analytically in a perturbation method. The electron microbunches forming on the scale of λ_r slip back through the radiation pulse and sequentially radiate the energy proportional to the FEL intensity overlapped by each microbunch. The field on the leading slope evolves along with n, and the exponent of the field function is proportional to the characteristic parameter $\rho_n=(3n-12)^{1/3}$ when the gain is much higher than the optical cavity loss. The gain decreases down to the level of cavity loss with increasing exponent, and a self-similar radiation pulse is generated at saturation. The characteristic parameter near the peak amplitude at saturation can be given by $\rho_s=2.8\alpha^{-1/3}$. The peak amplitude is determined by the optimum bunching on the scale of the radiation wavelength. The primary peak intensity of the intracavity optical radiation and the pulse length at saturation are found to scale with $(\rho/\alpha^{1/3})^4$ and $(\rho/\alpha^{1/3})^{-1}$, respectively, when both the incident rectangular electron bunch and slippage distance are longer than the distance from the front edge to the peak. Those scalings can account for the intense few-cycle FELs generated at the JAERI FEL in the high-gain and low-loss regime and provide a universal measure for generation of intense few-cycle FEL fields driven by synchronized electrons at various wavelengths.

ACKNOWLEDGMENTS

The author would like to acknowledge valuable discussions with T. Shizuma at JAERI, S. Hiramatsu at KEK, and H. Hama at Tohoku University.

[1] G. R. Neil, C. L. Bohn, S. V. Benson, G. Biallas, D. Douglas, H. F. Dylla, R. Evans, J. Fugitt, A. Grippo, J. Gubeli, R. Hill, K. Jordan, R. Li, L. Merminga, P. Piot, J. Preble, M. Shinn, T. Siggins, R. Walker, and B. Yunn, Phys. Rev. Lett. **84**, 662 (2000).

[2] H. Rabitz, R. de Vivie-Riedle, M. Motzkus, and K. Kompa, Science **288**, 824 (2000); D. J. Maas, D. I. Duncan, A. F. G. van der Meer, W. J. van der Zande, and L. D. Noordam, Chem. Phys. Lett. **270**, 45 (1997).

[3] G. Dattoli and A. Renieri, in *Laser Handbook*, edited by M. L. Stitch and M. Bass (North-Holland, Amsterdam, 1985), Vol. 4, p. 75.

[4] N. Piovella, P. Chaix, G. Shvets, and D. A. Jaroszynski, Phys. Rev. E **52**, 5470 (1995); P. Chaix, N. Piovella, and G. Grégoire, *ibid.* **59**, 1136 (1999).

[5] G. Dattoli and A. Renieri, Nuovo Cimento Soc. Ital. Fis., B **59**, 1 (1980); G. Dattoli, A. Marino, and A. Renieri, Opt. Commun. **35**, 407 (1980).

[6] W. B. Colson, in *Laser Handbook*, edited by W. B. Colson, C. Pellegrini, and A. Renieri (North Holland, Amsterdam, 1990), Vol. 6, pp. 115–193.

[7] Nicola Piovella, Phys. Rev. E **51**, 5147 (1995).

[8] H. Al-Abawi, F. A. Hopf, G. T. Moore, and M. O. Scully, Opt. Commun. **30**, 235 (1979); J. G. Kuper, G. T. Moore, and M. O. Scully, *ibid.* **34**, 117 (1980).

[9] D. A. G. Deacon, L. R. Elias, J. M. J. Madey, G. J. Ramian, H. A. Schwettman, and T. I. Smith, Phys. Rev. Lett. **38**, 892 (1977).

[10] R. Bonifacio, F. Casagrande, G. Oerchioni, L. De Salvo Souza, P. Pierini, and N. Piovella, Riv. Nuovo Cimento **13**, 1 (1990); R. Bonifacio, L. De Salvo Souza, P. Pierini, and N. Piovella, Nucl. Instrum. Methods Phys. Res. A **296**, 358 (1990).

[11] R. J. Bakker, D. A. Jaroszynski, A. F. G. van der Meer, D. Oepts, and P. W. van Amersfoort, IEEE J. Quantum Electron. **30**, 1635 (1994).

[12] N. Nishimori, R. Hajima, R. Nagai, and E. J. Minehara, Phys. Rev. Lett. **86**, 5707 (2001); Nucl. Instrum. Methods Phys. Res. A **483**, 134 (2002).

[13] R. Nagai, R. Hajima, N. Nishimori, N. Kikuzawa, M. Sawamura, and E. Minehara, Nucl. Instrum. Methods Phys. Res. A

483, 129 (2002).
[14] R. Hajima, N. Nishimori, R. Nagai, and E. J. Minehara, Nucl. Instrum. Methods Phys. Res. A **475**, 270 (2001); **483**, 113 (2002).
[15] C. A. Brau, *Free-Electron Lasers* (Academic, San Diego, 1990).
[16] Z.-W. Dong, K. Masuda, T. Kii, T. Yamazaki, and K. Yoshikawa, Nucl. Instrum. Methods Phys. Res. A **483**, 553 (2002).
[17] Ryoichi Hajima and Ryoji Nagai, Phys. Rev. Lett. **91**, 024801 (2003).
[18] Nobuyuki Nishimori, Nucl. Instrum. Methods Phys. Res. A **528**, 34 (2004).
[19] Norman M. Kroll and Wayne A. McMullin, Phys. Rev. A **17**, 300 (1978).
[20] W. B. Colson, J. C. Gallardo, and P. M. Bosco, Phys. Rev. A **34**, 4875 (1986).
[21] Nobuyuki Nishimori, Phys. Rev. ST Accel. Beams **8**, 100701 (2005).
[22] W. B. Colson and S. K. Ride, Phys. Lett. **76A**, 379 (1980).
[23] C. Penman and B. W. J. McNeil, Opt. Commun. **90**, 82 (1992).
[24] Kwang-Je Kim, Phys. Rev. Lett. **57**, 1871 (1986); Nucl. Instrum. Methods Phys. Res. A **250**, 396 (1986).
[25] N. Nishimori, R. Hajima, R. Nagai, and E. J. Minehara, Nucl. Instrum. Methods Phys. Res. A **507**, 79 (2003).
[26] W. B. Colson, in *Proceedings of the 23rd International Free Electron Laser Conference (FEL2001), Darmstadt, Germany, 2001* (Elsevier, Amsterdam, 2002), p. II-67.
[27] Roger W. Warren and John C. Goldstein, Nucl. Instrum. Methods Phys. Res. A **272**, 155 (1988).